EUSAR 2021 . ISBN 978-3-8007-5457-1 / ISSN 2197-4403 . ©VDE VERLAG GMBH . Berlin . Offenbach

Airborne SAR interferometry for large scale mapping of tidal flats: the GeoWAM project

Muriel Pinheiro[a], Rolf Scheiber[a], Joel Amao-Oliva[a], Marc Jaeger[a], Ralf Horn[a], Jens Fischer[a], Martin Keller[a], and Andreas Reigber[a]
[a]German Aerospace Center, Muenchener Strasse 20, Wessling, Germany

Abstract

Digital elevation models of tidal flats are a most valuable data source for the water management of coastal areas and need frequent updates to account for changes in sedimentation, erosion and identification of damages in building infrastructure. This paper presents the conceptual design, the processing methodology and first results of an airborne SAR campaign conducted in July 2019 at the German North Sea coast in the frame of the GeoWAM project, showing the potential for accurate monitoring height changes at decimeter level in mudflat areas, as well as indication of vegetation cover and water flooded areas.

1 Introduction

The water management of coastal areas influenced by tides requires regular high-resolution and accurate digital elevation models. Due to their very dynamic behavior, only extremely short time windows corresponding to +- 1 hour around the low tides are available for the remote data acquisition over areas of tidal flats. Hence, airborne sensors are more attractive than spaceborne ones due to their flexibility in terms of acquisition time. Moreover, high resolution airborne SAR systems – like the DLR-HR's F-SAR – have a wider footprint and are less dependent on weather conditions than conventional airborne laser scanner (ALS)s, which is usually limited to swath widths of <500m.

The work presented in this paper continuous on the initial developments on dual-frequency dual-baseline (DFDB) SAR interferometry presented in [1] and addresses improvements in data calibration, the mapping of wide areas by means of a mosaic consisting of several swaths and also the derivation of supplementary information for the indication of water covered areas or presence of vegetation, which might bias the derived elevation model.

The work is conducted within the governmental funded GeoWAM project, with partners from federal institutions, a SME, and universities. We shortly present the test-sites, the flight planning and DLR's F-SAR sensor configuration in section 2, the baseline selection trade-offs and theoretical performance figures in section 3, data processing details in section 4 and first preliminary results in section 5.

2 Campaign over the North Sea

Two test sites have been selected for the demonstration of topography retrieval via SAR interferometry for the monitoring of tidal flats. Both areas are located on the North Sea coast, in Germany. The first test site, Medemrinne, includes tidal flats of the Elbe river, whereas the second one, Otzumer Balje, is a gat (a waterway constantly affect by sedimentation/erosion) and includes the island of Spiekeroog. A first campaign was conducted in July, 2019 using the F-SAR system [2], which simultaneously acquired data in the S- and X- frequency bands in numerous passes over the two sites. The X-band data-set was acquired using VV polarization, while the S-band acquisitions were fully polarimetric. Moreover, each swath was imaged with the single-pass (SP) S- and X-band interferometers and, additionally, in a repeat-pass (RP) configuration with a nominal vertical baseline of 40 m. The use of the repeat-pass configuration is necessary due to the short single-pass baseline of the F-SAR (around 1.6 m), which by itself doesn't meet the challenging vertical resolution requirements. The use of different center frequencies is required to solve the processing challenges imposed by the relatively large repeat-pass baseline (which corresponds to heights of ambiguity of less than 2 m, see Section 4.2). The acquisition parameters used for both test data-sets are summarized in Table 1. For the Medemrinne test site, six par-

Parameter	X-band	S-band
Platform speed [m/s]	90	
Carrier frequency [GHz]	9.78	3.25
Transmitted bandwidth [MHz]	300	
Pulse repetition frequency (PRF) [Hz]	3800	1000
Range sampling frequency (RSF) [MHz]	500	
Pulse duration [μs]	9	
Azimuth resolution [m]	0.5	
Range resolution [m]	0.5	
Off-nadir angle [°]	25 to 55	
Single-pass (SP) vertical baseline [m]	1.5	
SP horizontal baseline [m]	0.4	
Repeat-pass (RP) vertical baseline [m]	40	
RP horizontal baseline [m]	0	
Mean height above ground [m]	2440	

Table 1 Parameters of the GeoWAM campaign over the North Sea, Germany.

allel swaths and a perpendicular one were acquired, each one with approximately 3 km x 12 km extension (covering an oevall area of around 165 km^2). For the Otzumer Balje test site, five parallel swaths and a perpendicular one were acquired, each one with approximately 3 km x 15 km extension (covering an overall area of around 155 km^2). Polarimetric images of the scene backscatter (S-band) for the two acquired mosaics are given in Figure 1 and Figure 2.

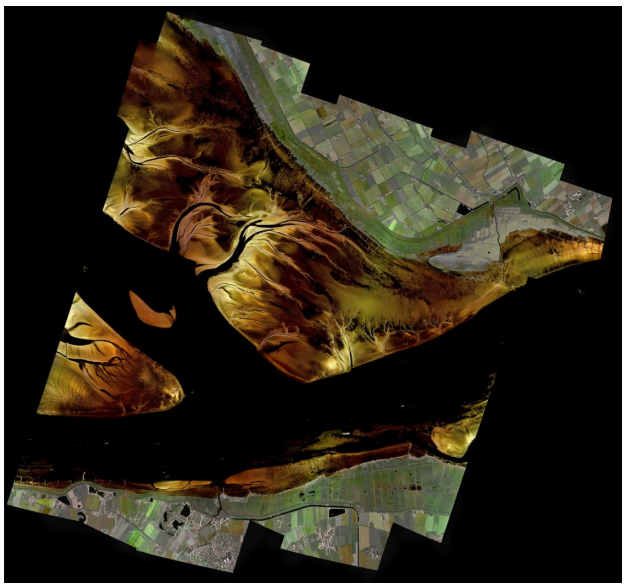

Figure 1 Polarimetric composite of the scene backscatter (S-band) for the Medemrinne test site.

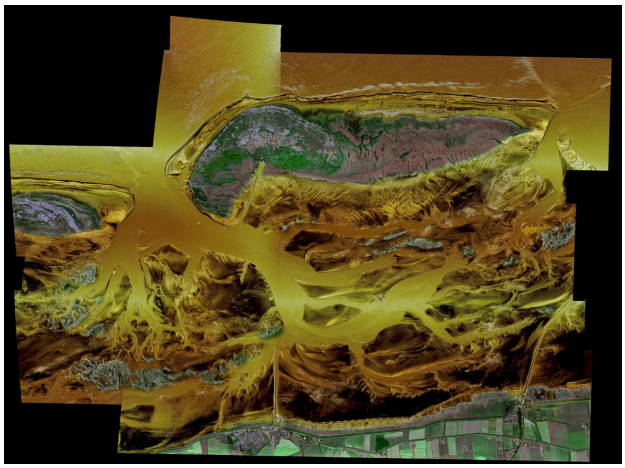

Figure 2 Polarimetric composite of the scene backscatter (S-band) for the Otzumer Balje test site.

3 Baseline selection and expected performance

For the monitoring of tidal flats, digital elevation models with both high resolution and high accuracy are required. In the GeoWAM project, the goal is to demonstrate the use of InSAR for the recovery of DEMs on a 1 m x 1 m grid and with relative and absolute vertical accuracy (2σ) in the order of decimeters (ideally smaller than 30 cm). The desired relative vertical accuracy is only theoretically possible if the interferometric baseline is sufficiently large. On the other hand, the spectral shift should be kept to a minimum in order to preserve the range resolution. Moreover, very large baselines correspond to very small heights of ambiguity (e.g., less than 1 m), which are problematic due to the inevitable introduction of phase unwrapping errors. Hence, the baseline cannot be excessively large.

In order to choose the appropriate repeat-pass baseline, a performance analysis has been conducted. The analysis modeled the geometry of the repeat-pass acquisition as defined by the altitude above ground of the master acquisition plus the horizontal (Bh) and vertical (Bv) separation to the slave, as shown in Figure 3. A few options for Bh and Bv were considered (see Table 2), and the corresponding height of ambiguity, spectral shift and, eventually, height sensitivity were assessed. In all cases, we considered an output grid with 1 m x 1 m sampling, an altitude above ground of around 2400 m, and a valid off-nadir range from 25° to 55°. The sensitivity analysis assumes

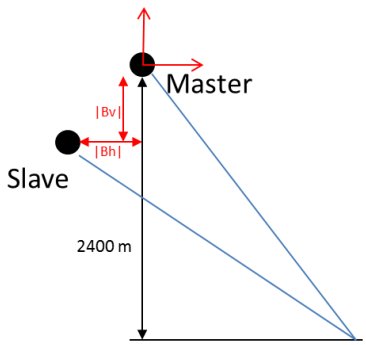

Figure 3 Repeat-pass acquisition geometry.

that the only sources of decorrelation are the signal-to-noise ratio (SNR) and the temporal decorrelation, i.e., we assume that a range-filter has been applied to compensate for geometrical decorrelation, and volume decorrelation is neglected. This last assumption is reasonable for tidal flats, where penetration in X- and S-band is considered negligible. However, it is not valid for semi-transparent media. Hence, the sensitivity analysis carried out in the following does not apply to vegetated areas or very dry sand. The SNR decorrelation was predicted considering Noise-Equivalent-Sigma-Zero (NESZ) estimated from previous F-SAR campaigns and considering backscatter values ranging from 0 to -25 dB (fixed over the swath). The temporal decorrelation was assumed to be 0.8 and 0.7 for S- and X-band repeat-pass data, values which were also obtained from previous F-SAR campaigns over the North Sea [1].

Figure 4 shows the expected height of ambiguity and spectral shift for the five cases in Table 2. The effective baseline of case 1 is too large, resulting in a spectral shift of more than 200 MHz for incidence angles smaller than 35°, and height of ambiguity smaller than 0.5 m at near range. Case 2 and case 3 present similar metrics, with case 3 having slightly less performance variation along the swath. Both cases have a relative small height of ambiguity at near range. Case 4 and 5 show less variation of the height of

	Bh	Bv
Case 1	-30	-30
Case 2	-20	-20
Case 3	-10	-30
Case 4	0	-40
Case 5	10	-40

Table 2 Options of vertical and horizontal repeat-pass baseline.

ambiguity with range and spectral shifts of 170 MHz and 60 MHz at 25°. Hence, they are considered more appropriate for the reconstruction of the elevation models of the tidal flats, and are taken as candidates for the sensitivity evaluation shown in Figure 5. For backscatters coefficients ranging from 0 to -15 dB, both cases allow for 2σ<50cm. Case 5 has worse performance in general, and for the -25dB backscatter case, its accuracy goes beyond 50 cm for both near- and far-range. On the positive side, it presents more homogeneous performance within the swath in comparison to case 4.

The real flight trajectory deviates from the ideal one, leading to baseline errors up to +- 2m for the horizontal component and up to -+ 6m for the vertical component in the case of the F-SAR carrier. As a consequence, the expected DEM performance will also vary along azimuth. Note that baseline errors are more critical for case 5, since its performance was already close to the assumed threshold. Moreover, since the positive horizontal baseline cause a non-negligible worsening of the performance at near-range, and can, in extreme cases, lead to invalid data due to the alignment of master and slave with the line-of-sight, the optimal baseline choice among the considered ones is the one of case 4, i.e.[0,-40] m.

Finally, the analysis suggests that the S-band DEM has a worse expected performance than the X-band one due to the increased wavelength. However, this should not impact the quality of the final estimated repeat-pass DEM, since the merging of X- and S-band information accounts for the individual DEM statistics, and the relative accuracy of the resulting DEM should be at least as good as the X-band one [1].

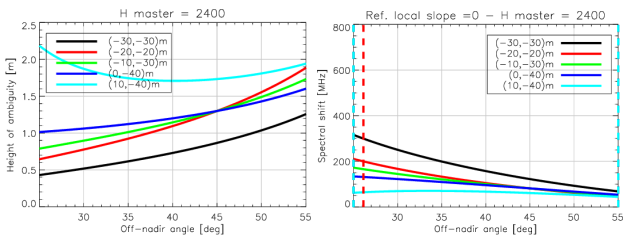

Figure 4 Expected X-band (left) height of ambiguity and (right) spectral shift for the different baseline configurations.

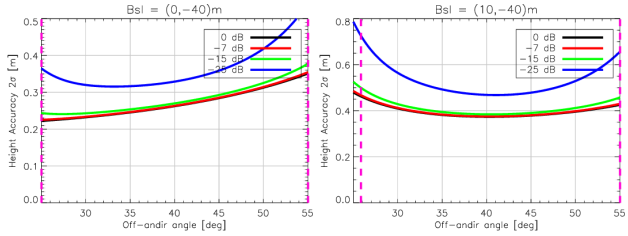

Figure 5 Expected X-band height accuracy (left) case 4 and (right) case 5 for different SNR. The magenta lines mark the valid swath considering an accuracy requirement of 30 cm (2σ).

4 Data Processing

4.1 SAR focusing and calibration

Dedicated acquisitions over the F-SAR calibration site at Kaufbeuren, Germany were used to derive calibration corrections for the processing of SAR data gathered in the field. The calibration site features nine trihedral radar reflectors and one dihedral reflector deployed at off-nadir angles ranging between 20° and 60°. The responses of these reference targets were used as input to the calibration procedure described in [3] and [4], which yields, among other things, precise antenna phase centre baselines for the S- and X-band single-pass interfeometers as well as calibration constants for the range delays, the channel gains and the inter-channel phase differences.

In addition, the calibration included the estimation of a residual antenna phase error to correct for small phase inaccuracies in the on-ground characterisation of the antenna patterns. This estimate was carried out using phase differences measured over distributed targets in the range-Doppler domain to yield a 2D phase correction, in terms of off-nadir angle and squint, for each slave antenna of the S- and X-band interferometers. The squint-variant estimate helped to ensure that the correction is applicable for all acquisition geometries encountered in the field.

4.2 DEM Generation

The DEM generation is based on the Dual-frequency/Dual-baseline (DFDB) chain introduced in [1] and [5], and considers a few simplification in the calibration procedure. The main steps of the chain and main differences to the scheme in [1] are summarized in the following.

4.2.1 Generation of interferometric products

The first step is the generation of the interferometric products. A range-adaptive spectral filter is applied to the repeat-pass data and a mean reference height is considered for the flattening. The multi-squint approach is applied for the correction of residual motion errors in the repeat-pass interferograms (up to constant and linear components) [6]. The estimation is performed using the data from a single frequency of acquisition (X-band preferably), and applied to both data-sets. After the interferograms have been formed, the interferometric phase and coherence are ex-

tracted and are interpolated to the geometry of the X-band master image.

4.2.2 Dual-frequency phase unwrapping

The second step is the unwrapping of the interferometric phases and is performed using the dual-channel region-growing approach we suggested in [5].

4.2.3 Baseline calibration

After the phase unwrapping, a calibration step is performed. Unlike our previous strategy in [1], the estimation of multi-path artefacts caused by a secondary reflection on the aircraft fuselage is not applied for the GeoWAM data. This is because the F-SAR processing chain now includes the estimation of a residual antenna phase screen which accounts for this effect. This estimation is performed offline using data from calibration campaigns (see Section 4.1), and is considered to be accurate enough for achieving the desired absolute accuracy.

The calibration performed at this stage then accounts only for constant and linear baseline errors and a global offset. The strategy adopted here is a simplified version of the baseline calibration we presented in [1]. This is because ground control points (GCPs) were measured *in situ* during the GeoWAM campaign. This information allows for the estimation of the global offset affecting the single-pass interferograms and, consequently, for a better conditioning of the repeat-pass calibration problem [1]. Since the GCPs are not available for the whole imaged polygon, only the perpendicular stripe is calibrated, at a first stage. The calibration of the interferograms from the remaining stripes is performed considering the DEM derived from this perpendicular stripe.

4.2.4 Correction of unwrapping errors

After the trends and global offsets have been calibrated, unwrapping errors are detected and corrected using the DFDB active-contours-based approach we presented in [1].

4.2.5 Phase-to-height conversion

In the next step, the calibrated phases are individually transformed to height maps, still in slant-range geometry, and the expected height error maps based on the interferometric coherences are calculated. At this point in the chain, we have the height maps (and height error maps) corresponding to single-pass X-band, single-pass S-band, repeat-pass X-band and repeat-pass S-band.

4.2.6 Residual calibration

At this stage, the repeat-pass data-sets are still impacted by uncompensated low-frequency artefacts. These might originate from atmospheric disturbances, but can also be related to limitations of the residual motion compensation algorithm (e.g., due to the presence of large incoherent areas spanning through the whole imaged swath). Hence, a residual calibration step is performed after the height conversion. The strategy is based on the one presented in [1], i.e., we consider the residual errors in X- and S-band height maps correlated.

4.2.7 Generation of combined repeat-pass height map

At this stage, the X-band and S-band repeat pass interferograms are merged into the final elevation model considering a wavelet-based noise mitigation strategy as described in [1]. However, in the GeoWAM project we do not merge the information of SP and RP interferograms, i.e., the combined RP DEM will be marked as invalid for flooded areas, whereas the SP one might contain the information of the water level (depending on the roughness of the water surface).

4.2.8 Geocoding

The retrieved height maps can now be interpolated back to their master geometry (when necessary). The last step of the DFDB chain for a single stripe is the geolocation of the obtained SP, RP and combined elevation models, i.e., their transformation from radar geometry to UTM coordinates.

4.2.9 Mosaicking

Since several stripes are available, the final stage of the "DEM Generation" is the mosaicking of the available products. The procedure takes into consideration the expected relative height errors derived in the "Phase-to-height conversion" step and, additionally, considers feathering in order to avoid border artefacts [7].

4.3 Auxiliary masks for data interpretation

In addition to the derived DEMs, the monitoring of the tidal flats using InSAR can also profit from the availability of the SAR amplitude and coherence maps, and from the fully polarimetric information available in S-band. In the following, we describe the generation of an interferometry and a polarimetry mask which will aid on the interpretation of the land cover.

4.3.1 Interferometry mask

The interferometry mask uses the information of the S-band VV amplitude of master and slave, as well as the repeat-pass coherences, and it can help on the separation of flooded areas from non-flooded ones. The repeat-pass coherence is useful for the separation of water from ground, since water completely decorrelates in repeat-pass interferograms. However, semi-transparent media (e.g., forests or crops) and areas with steep surface topography changes (e.g., buildings) also tend to present very low coherence in the repeat-pass interferograms. On the other hand, such targets tend to present higher amplitudes, which are stable in master and slave acquisition passes. Finally, tidal mudflats tend to present low amplitude and can correspond to low or high coherence in the repeat-pass interferograms, depending on the water dynamics and moisture. Note that, due to the tidal dynamics, the water level might vary from master to slave pass. Hence, for the data interpretation it is important to consider both amplitudes.

The generation of the interferometry mask has mainly two

Class	RP Coh	Master Amp	Slave Amp	Possible interpretation
0	low	low	low	Water, shadow, crops
1	low	low	high	Mudflat, under water for master pass
2	low	high	low	Mudflat, under water for slave pass
3	low	high	high	Vegetation, crops and buildings
4	high	low	low	Dry tidal flat
5	high	low	high	Unlikely
6	high	high	low	Unlikely
7	high	high	high	Ground

Table 3 Classes of the interferometry mask. Depending on wind effects on water, classes 1 and 2 can be reversed.

steps. The first one is the computation of amplitude and coherence thresholds which will be used to differentiate between coherent and incoherent regions, and between incoherent regions with low or high amplitudes. The second step is the actual generation of the mask according to the classes defined in Table 3. After the assignment of the classes, a morphological opening is applied to mitigate the effects of estimation biases in low coherence areas.

For the computation of coherence threshold, the histogram of the repeat-pass coherence of the whole acquired mosaic is computed. Typically, two main maxima are identified, and the threshold is set at the inflection point in between these lobes. For the computation of the amplitude threshold, only areas of low coherence are considered (identified by the previously calculated coherence threshold). The goal here is to separate the maxima with highest amplitude – which typically corresponds to vegetated and urban areas – from the remaining ones. Figure 6 shows the obtained coherence and amplitude histograms for the Otzumer Balje test site, and indicates the estimated thresholds.

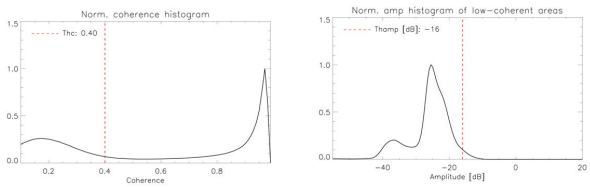

Figure 6 (Left) coherence and (right) amplitude histograms for the Otzumer Balje test site.

4.3.2 Polarimetry mask

In the case of the polarimetry mask, the standard entropy-alpha unsupervised classification scheme was performed [8]. The entropy-alpha classifier utilizes the polarimetric information that is not considered in the interferometry mask. This allows for the reduction of classification ambiguity present in some of the classes of the interferometry mask (namely, in classes 4 and 0), where the vegetation present in the upper part of the image (see Figure 7) is being incorrectly classified as dry tidal flat, for example.

A small modification on the ordering of the original entropy-alpha classes was performed, going from low to high entropy within the same type of reflection (see Table 4). This reordering step is necessary since feathering on overlapping classes is not defined. For the mosaicking of labels, a ceiling approach (taking the highest class value on overlapping pixels) is applied instead of border feathering, prioritizing the preservation of high entropy classes. Nonetheless, some areas of the polarimetric mask are still affected by different water levels and incidence angles leading to residual border effects during the mosaicking.

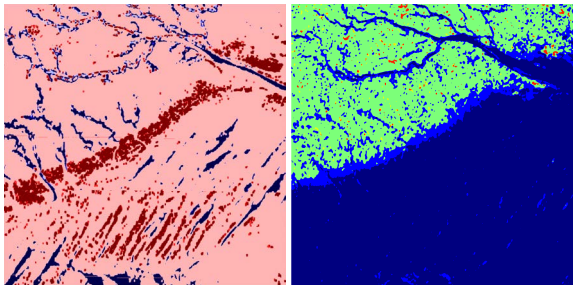

Figure 7 Interferometry mask (left) classification ambiguity resolved using S-band polarimetric information present in the polarimetry mask (right). The blue colors in the polarimetric mask correspond to surface classes [0,1 and 2], while the green and red colors correspond to vegetation and multiple scattering classes, respectively.

Class	Entropy	Type of Reflection	Possible Class Interpretation
0	low	surface	Water, mudflat
1	medium	surface	Water, mudflat
2	high	surface	Water with wind
3	low	dipole	Vegetation with oriented structure
4	medium	vegetation	Short vegetation (grass)
5	high	vegetation	Tall vegetation
6	high	multiple	Tall vegetation (trees)
7	medium	multiple	Buildings
8	low	multiple	Buildings

Table 4 Classes of the polarimetry mask.

5 Preliminary results

In this section, preliminary results from the Otzumer Balje test site are shown. Figure 8 shows the retrieved X-band single-pass DEM. Figure 9 shows a few zooms of the repeat-pass S-band DEM for regions where topography changes were observed in comparison to an ALS DEM acquired in 2014. The figure also includes the reference ALS and the difference between both models. Figure 10 shows the interferometry mask, whereas Figure 7 shows the complementarity of the polarimetry mask for a tile of 1 square km size.

6 Summary

This paper presented an overview of the GeoWAM project which aims for monitoring of tidal flats by means of SAR interferometry. Whilst the project is ongoing, we presented the adopted SAR processing approach and first results demonstrating the potential for deriving accurate high resolution DEMs as well as supplementary information like indication of water flooded areas and vegetation cover.

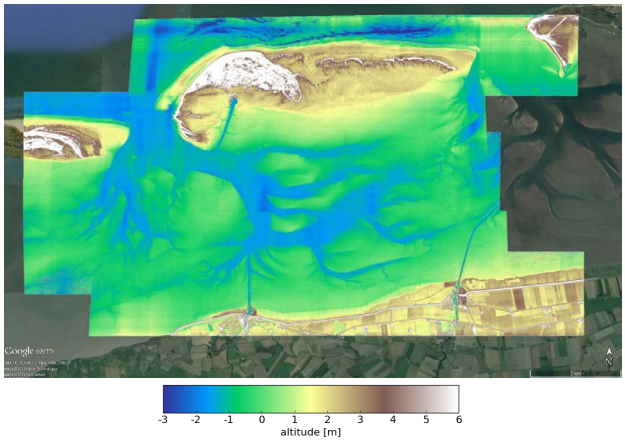

Figure 8 Single-pass X-band DEM of the Otzumer Balje test site.

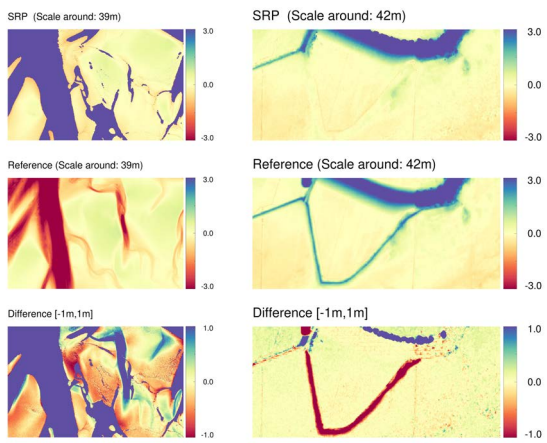

Figure 9 Zooms of the S-band RP DEM of the Otzumer Balje test site over areas where topography changes were observed in comparison to an ALS DEM acquired in 2014.

7 Acknowledgement

The GeoWAM project is funded by the German Federal Ministry of Transport and Digital Infrastructure (BMVI) within the framework of the Modernity Fund ("mFUND") funding directive with a total of 2.25 MEuro. The authors acknowledge the fruitful cooperation within the project consortium which includes the German Federal Office of Hydrology (BfG), the Lower Saxony State Department for Waterways, Coastal and Nature Conservation (NLWKN), disy GmbH, and the Universities of Stuttgart and Karlsruhe.

8 Literature

[1] M. Pinheiro, A. Reigber, R. Scheiber, P. Prats-Iraola, and A. Moreira, "Generation of Highly Accurate DEMs Over Flat Areas by Means of Dual-Frequency and Dual-Baseline Airborne SAR Interferometry," *IEEE TGRS*, vol. 56, no. 8, pp. 4361–4390, Aug 2018.

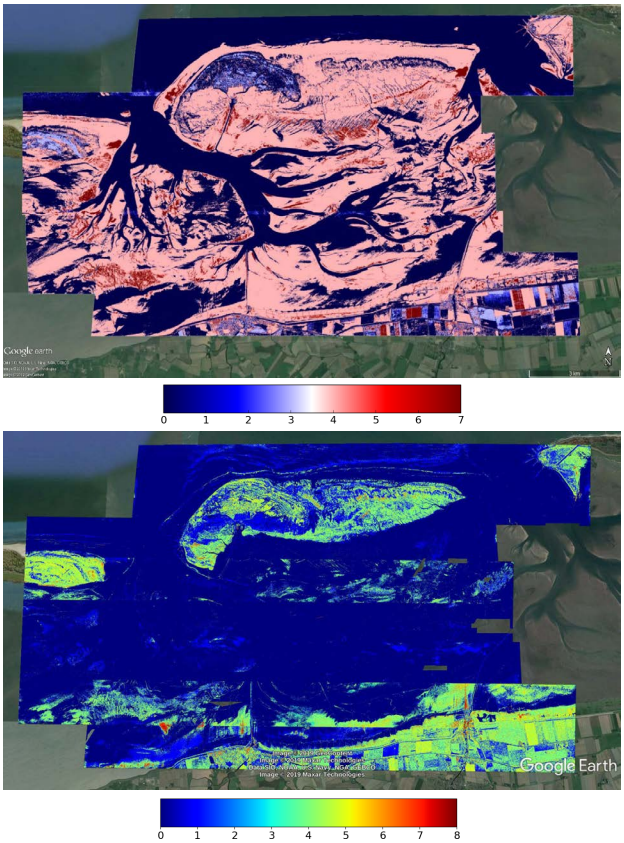

Figure 10 Interferometry (top) and polarimetry (bottom) masks computed for the Otzumer Balje test site.

[2] R. Horn, A. Nottensteiner, A. Reigber, J. Fischer, and R. Scheiber, "F-SAR - DLR's new multifrequency polarimetric airborne SAR," in *Geoscience and Remote Sensing Symposium (IGARSS), Proceedings of 2009 IEEE International*, vol. 2, July 2009, pp. 902–905.

[3] M. Jäger, R. Scheiber, and A. Reigber, "External calibration of multi-channel sar sensors based on the pulse-by-pulse analysis of range compressed data," in *EUSAR*. VDE, June 2018. [Online]. Available: https://elib.dlr.de/115351/

[4] ——, "Robust, model-based external calibration of multi-channel sar sensors using range compressed raw data," *Remote Sensing*, Submitted 2019.

[5] M. Pinheiro, A. Reigber, and A. Moreira, "Large-baseline InSAR for precise topographic mapping: a framework for TanDEM-X large-baseline data," *Advances in Radio Science*, vol. 15, pp. 231–241, 2017.

[6] A. Reigber, P. Prats, and J. Mallorqui, "Refined estimation of time-varying baseline errors in airborne SAR interferometry," *Geoscience and Remote Sensing Letters, IEEE*, vol. 3, no. 1, pp. 145–149, Jan 2006.

[7] A. Gruber, B. Wessel, M. Martone, and A. Roth, "The TanDEM-X DEM Mosaicking: Fusion of Multiple Acquisitions Using InSAR Quality Parameters," *IEEE JSTARS*, vol. 9, no. 3, pp. 1047–1057, March 2016.

[8] S. R. Cloude and E. Pottier, "An entropy based classification scheme for land applications of polarimetric SAR," *IEEE Transactions on Geoscience and Remote Sensing*, vol. 35, no. 1, pp. 68–78, Jan 1997.